

# A Unique Quenching and Deformation Dilatometer for Combined In Situ Neutron Diffraction Analysis of Engineering Materials

Xiaohu Li,\* Michael Hofmann, Martin Landesberger, Marius Reiberg, Xiao Zhang, Yuanding Huang, Lijiu Wang, Ewald Werner, and Weimin Gan\*

A modified quenching and deformation dilatometer (TA instruments DIL 805A/D/T) is now in operation at the Heinz Maier-Leibnitz Zentrum (MLZ, Germany) neutron center. It is customized for running neutron scattering measurements during the temperature/deformation treatment of the sample, in particular neutron diffraction (phase, texture, and lattice strain) and neutron small angle scattering. The bulk length change of dilatometer specimens is successfully combined with in situ neutron diffraction patterns for analyzing dynamic processes in metallic materials. A detailed introduction to the unique dilatometer is given and examples of recent experiments highlight the use of the added insight provided by combining diffraction and dilatometry.

## 1. Introduction

Thermal analysis (TA) is a standard technique to study the chemical and physical properties of materials as they change with temperature. For the development of new alloys and improvement of existing engineering materials, TA is essential to understand material behavior under the influence of thermal loads, to predict

its performance, and to optimize processing conditions. A TA instrumentation normally comprises a furnace, a temperature measurement setup, and a corresponding data recording unit. In addition, to study material property changes in the sample under applied force (tension, compression, bending, etc.) thermomechanical analysis (TMA) is applied. A dilatometer is a sufficiently precise equipment that can be applied to perform both TA as well as TMA experiments. Typical dilatometry measurements include the determination of thermal expansion, monitoring phase transitions, conducting kinetics studies,

constructing phase diagrams, performing sintering studies, and many more. Dilatometry utilizes the volume change associated with nearly all solid material transitions and measures the length change of a specimen as it is heated and cooled at a fixed rate.<sup>[1]</sup> Modern dilatometers offer a high resolution measurement of length change ( $\Delta l$ ), which can reach a length change resolution down to  $\Delta l \approx 1$  nm in case of the DIL 831 manufactured by TA instrument.<sup>[2]</sup> Moreover, the sensitivity in length change can be maintained also during long-term isothermal measurement conditions.<sup>[3]</sup> In addition, compared to conventional laboratory furnaces, a dilatometer can provide a very wide range of heating/cooling rates from typically  $0.001 \text{ K s}^{-1}$  up to  $1000 \text{ K s}^{-1}$ .<sup>[4]</sup>


Initially, dilatometry has been widely used in studying the kinetics of austenite–ferrite phase transformations.<sup>[4]</sup> Application of dilatometry for constructing continuous heating transformation (CHT) and continuous cooling transformation (CCT) diagrams of steels has been outlined as a main source to understand the transformation behavior.<sup>[5]</sup> These diagrams have shown that the knowledge of microstructural constituents resulting from given heating and cooling conditions is instrumental for the metallurgist in steel characterization and production. Dilatometry measurements have also been used deriving time–temperature–precipitation (TTP) diagrams. For ferrous materials, a wide range of TTP diagrams which include the information of isothermal transformation, CCT, TTP, time–temperature embrittlement, and time–temperature ordering have been collected.<sup>[6]</sup> A detailed study of precipitation kinetics of a dilute Al–Mg–Si under isothermal dilatometry has revealed the evolution of the atomic fraction of two precipitates.<sup>[7]</sup> The result was used to construct the isothermal TTP diagrams which can be incorporated into technologically relevant processes. Using a

Dr. X. Li, Dr. W. Gan  
GEMS at MLZ  
Helmholtz-Zentrum Geesthacht  
D-85748 Garching, Germany  
E-mail: xiaohu.li@hzg.de; weimin.gan@hzg.de

Dr. M. Hofmann, M. Landesberger, L. Wang  
Heinz Maier-Leibnitz Zentrum (MLZ)  
Technische Universität München  
D-85748 Garching, Germany

M. Reiberg, Prof. E. Werner  
Institute of Materials Science and Mechanics of Materials  
Technische Universität München  
D-85748 Garching, Germany

X. Zhang, Dr. Y. Huang  
Institute of Metallic Biomaterials  
Helmholtz-Zentrum Geesthacht  
D-21502 Geesthacht, Germany

 The ORCID identification number(s) for the author(s) of this article can be found under <https://doi.org/10.1002/adem.202100163>.

© 2021 The Authors. Advanced Engineering Materials published by Wiley-VCH GmbH. This is an open access article under the terms of the Creative Commons Attribution License, which permits use, distribution and reproduction in any medium, provided the original work is properly cited.

DOI: 10.1002/adem.202100163

quenching dilatometer at extraordinarily long isothermal aging times, the temperature–time–transformation (TTT) curves have been obtained for both a primary precipitation and an eutectoid decomposition in a Cu–Al–Ni shape memory alloy.<sup>[8]</sup> In this article, crystal structures of the precipitate and the decomposition phase were also identified in the quenched samples using X-ray diffraction. A method using the dilatometric signal, assuming isotropic dilatation and considering atomic volumes of the phases present, in this case austenite and bainitic ferrite, finally lead to an estimation procedure for the dislocation density.<sup>[9]</sup> In this article, ex situ quantitative X-ray diffraction analysis was needed in addition for determination of the fraction of retained austenite and bainitic ferrite.

To combine diffraction and TA, a quenching/deformation dilatometer is available since 2011 at the high energy X-ray beamline High Energy Materials Science (HEMS) at Deutsches Elektronen-Synchrotron center in Germany.<sup>[10]</sup> Using this dilatometer together with in situ synchrotron X-ray diffraction, the CCT behavior of two low-alloy vessel steels was investigated across a range of cooling rates following austenitization.<sup>[11]</sup> This study revealed a good agreement in transformation start temperatures between the two techniques and helped to correct the length change signal from dilatometer for ferrite phase quantification, thereby avoiding overestimation. For the first time, an in situ synchrotron experiment using this dilatometer was performed during the solidification of Mg–4Y–3Nd alloy to determine the solidification sequence of the phases and to correlate them with the thermodynamic simulations.<sup>[12]</sup> However, in this experiment, the dilatometer was only used as a high precision furnace without using the information of length change. To date, a large number of dilatometric studies have been performed at the HEMS beamline on the lightweight intermetallic TiAl alloys.<sup>[13]</sup> Combining the information from dilatometry with in situ high energy X-ray diffraction allowed tracing the evolution of phase fractions of these alloys over a wide temperature range. However, the order–disorder transition in TiAl alloys cannot be detected unambiguously using synchrotron radiation alone due to the equal X-ray scattering lengths of Ti and Al atoms. Moreover, so far the maximum beam size of high energy X-ray can only reach about 1 mm<sup>2</sup> which provides insufficient grain statistics for materials with coarse and/or lamellar grains. Furthermore, photoabsorption strongly depends on the atomic number, which limits its application for materials containing heavy elements such as tungsten, cobalt, and niobium.

Therefore, to overcome these limitations, the installation of a modified dilatometer for neutron scattering was initiated at Maier-Leibnitz Zentrum (MLZ), first for the two beamlines STRESS-SPEC (diffraction) and SANS-1 (small angle scattering). In particular, neutron diffraction is a powerful tool to probe structural chemistry of solid-state materials. Since neutrons are scattered from nuclei, neutron diffraction offers additional advantages compared to X-rays such as providing a different contrast for elements and a high penetration depth of several centimeters. As neutron beam size at a diffractometer can be quite large, neutrons are quite well suited for the investigation of samples with coarse or lamellar grains. In addition, in situ analysis using bulky sample environment such as a dilatometer is easily possible with neutrons. In recent years, diffraction-based in situ analysis techniques have been developed increasingly.<sup>[14]</sup>

This is because in situ diffraction with neutron or synchrotron radiation offers the possibility to investigate real-time structural evolutions on the atomic scale. In particular, crystal structure and phase fraction, preferred orientation/texture and lattice strain can be derived.

Therefore, in the past few years, various devices or components have been developed at currently available worldwide materials/engineering neutron diffractometers to facilitate in situ neutron diffraction during thermomechanical processing. This includes devices such as specialized load frames including rapid infrared heating at the diffractometer ENGIN-X (ISIS, UK) or induction heating at the neutron strain scanner VULCAN (SNS, USA), respectively.<sup>[15,16]</sup> A quite unique instrumentation is the thermomechanical processing simulator at BL19 TAKUMI (J-PARC, Japan).<sup>[17]</sup> Using this particular device, many studies related to phase transformations kinetic, texture evolution, and developing mechanical properties in alloys have been conducted successfully in recent years, highlighting the demands for this kind of in situ studies.<sup>[18–21]</sup> Compared to these thermomechanical devices, the dilatometer is used as a phase transition research equipment including loading and heating/quenching in one device with an exceptionally resolution of the sample length change. It offers highly stable and accurate temperature control and, as instrumentation of this type is also used in many material laboratories as standard equipment for kinetic studies of phase transitions, it is common to a wider user community.

The report at hand presents the specifications and capabilities of our unique experimental setup. The advantages of combining dilatometry with neutron diffraction for studying modern materials are demonstrated for three typical measurements at the engineering materials science diffractometer STRESS-SPEC at MLZ.

## 2. The Quenching/Deformation Dilatometer

The current DIL 805A/D/T dilatometer is a modified device from TA Instruments, which can realize quenching in combination with deformation (compression and tension). Its bulk length change signal is detected via a push rod made of glass or alumina. Push rod dilatometry is a well-proven method for characterizing dimensional changes of a material as a function of temperature. The measurement may be performed across a wide temperature range (e.g., from room temperature [RT] to 1500 °C), or employing a user-defined temperature program to simulate industrial processes, firing regimes, or a material's operating environment. The coefficient of thermal expansion ( $\alpha$ ) is defined as the normalized expansion ( $\Delta l/l_0$ ) divided by the change in temperature ( $\Delta T$ ).

### 2.1. Design and Specifications

The sample deformation such as thermal expansion and contraction with changing temperature is measured as the probe displacement by the length detector. A linear variable differential transformer (LVDT) is used for this length detection sensor. The modified dilatometer used in our investigations has a length resolution of up to 10 nm using the “alpha” measuring unit. To the best of our knowledge, this is the highest length resolution achievable currently in in situ neutron diffraction.

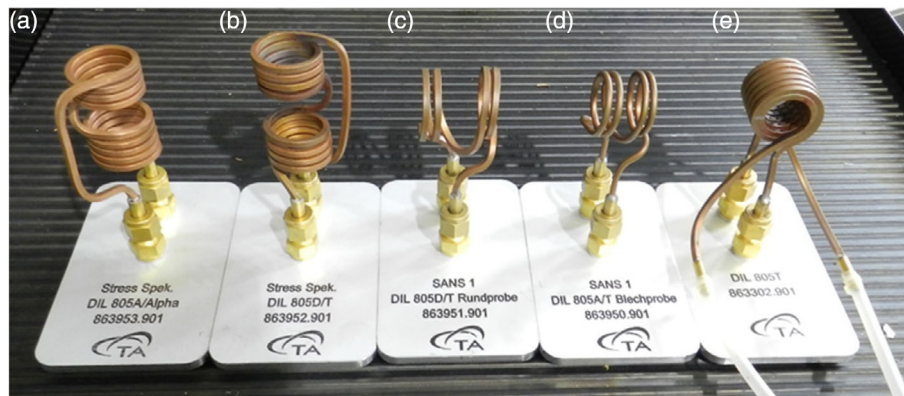


**Figure 1.** Uniquely designed induction coils for the STRESS-SPEC neutron diffractometer and the SANS-1 neutron small-angle scattering beamline, respectively. The induction coils from left to right are as follows: a) STRESS-SPEC alpha/quenching mode, b) STRESS-SPEC deformation mode, c) SANS-1 deformation mode for cylindrical samples, d) SANS-1 quenching/tension mode for sheet samples, and e) standard induction coil.

The sample temperature change is controlled by an oscillator, which is connected to an induction coil. To cooperate with the geometries of neutron diffraction at STRESS-SPEC and in a later stage also for neutron small angle scattering, four new induction coils have been specially designed for this purpose, as shown in **Figure 1**. The middle part of the induction coil is separated to avoid shielding both the incoming and outgoing neutron beam with a typical beam size of  $5\text{ mm} \times 5\text{ mm}$ . Unfortunately, such a design weakens the induced magnetic field generated by the induction coil, thus making the highest reachable sample temperature lower than the  $1500\text{ }^\circ\text{C}$  which can be reached using a standard induction coil (**Figure 1e**). However, this modification does not change its excellent temperature control accuracy. Compared to other thermomechanical devices, these uniquely designed induction coils reduce the fluctuation between target and sample temperature caused by over heating/over cooling at the end of fast heating/quenching stage to  $\pm 3\text{ }^\circ\text{C}$  within  $5\text{ s}$ .<sup>[20,21]</sup> The maximum sample temperature is further affected by the relative permeability  $\mu/\mu_0$  of sample material itself. For example, an alloy containing a large amount of a phase with low relative permeability  $\mu/\mu_0 \leq 1$  can only be heated to a maximum temperature of about  $800$  to  $1000\text{ }^\circ\text{C}$  using the new dilatometer in deformation mode. When using the quenching mode alone maximum temperatures of  $\approx 1400\text{ }^\circ\text{C}$  for TiAl, and  $1300\text{ }^\circ\text{C}$  for Co-based alloy can be reached with the modified coils.

**Table 1.** Specification and parameters of dilatometer using specially designed STRESS-SPEC induction coils.

Type of mode	Alpha/quenching	Compression	Tension
Temperature range	50 to $1400\text{ }^\circ\text{C}$ (depends on material and modes)		
Temperature resolution		$0.05\text{ }^\circ\text{C}$	
Heating rate	$100\text{ K s}^{-1}$	$60\text{ K s}^{-1}$	$40\text{ K s}^{-1}$
Cooling rate	$150\text{ K s}^{-1}$	$150\text{ K s}^{-1}$	$100\text{ K s}^{-1}$
Length change accuracy	$10\text{ nm}/50\text{ nm}$	$50\text{ nm}$	$50\text{ nm}$
Deformation force		Max. $20\text{ kN}$	Max. $8\text{ kN}$
Deformation rate		$0.01\text{--}200\text{ mm s}^{-1}$	$0.01\text{--}20\text{ mm s}^{-1}$
Strain rate		$0.001\text{--}20\text{ s}^{-1}$	$0.001\text{--}20\text{ s}^{-1}$

Parameters related to the measurement process of the dilatometer in four different modes are summarized in **Table 1**.

The sample geometry used in tension mode is shown in **Figure 2** (with more detailed drawings available in ref. [22]). The sample temperature is measured by a thermocouple spot welded onto the sample surface and the heat treatment can be performed in vacuum or in inert gas  $\text{N}_2/\text{He}$  atmosphere. The maximal cooling rate shown in **Table 1** is reached from  $1500\text{ }^\circ\text{C}$  down to around  $100\text{ }^\circ\text{C}$  using He gas flow. Below  $100\text{ }^\circ\text{C}$ , the maximum cooling rate will continue to decrease gradually until quenching to RT. Mechanical deformation loading is facilitated by a hydraulic oil actuator acting on ceramic or steel pistons (further details can be found in ref. [23]).

## 2.2. Integration into the Instrument

The dilatometer is designed so that it can be used like the usual standard sample environment available at the neutron diffractometer. This includes that it can be easily installed or uninstalled as well as quickly aligned to the neutron beam. It is mainly installed at the STRESS-SPEC instrument, which is an optimized engineering materials science neutron diffractometer at MLZ. STRESS-SPEC offers highly flexible setup options for the respective measurements purpose.<sup>[24]</sup> It also provides variable specialized sample environments such as a mirror furnace and a tension/compression rig which can be combined with in situ neutron diffraction.<sup>[25]</sup>

Utilizing an adapter to the  $xyz$ -stage with a load capacity of  $\approx 300\text{ kg}$ , the dilatometer can be mounted so that the centre of a cylindrical sample to be tested is located around the neutron beam gauge centre. Since the standard specimen for the dilatometry test has cylindrical geometry with a diameter of  $5\text{ mm}$  and a height of  $10\text{ mm}$ , the current standard gauge volume for measurements is set to about  $5 \times 5 \times 5\text{ mm}^3$  using a specialized radial collimator in front of the detector, as shown in **Figure 3**. This setup ensures that only the sample is visible to the neutron beam during a measurement and no additional diffraction signals are recorded from the sample environment. A 2D position sensitive  $^3\text{He}$  detector (PSD) with  $25 \times 25\text{ cm}^2$ ,  $256 \times 256$  pixels, and a  $2\theta$

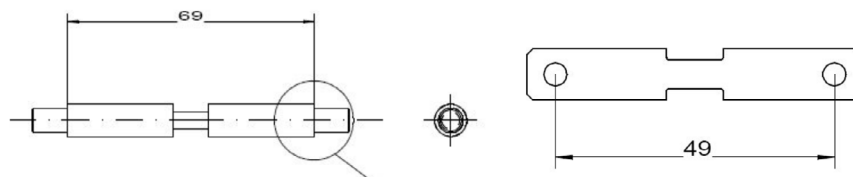


**Figure 2.** Geometry of tension samples used for dilatometer experiment. Left: cylindrical sample. Right: flat sample.

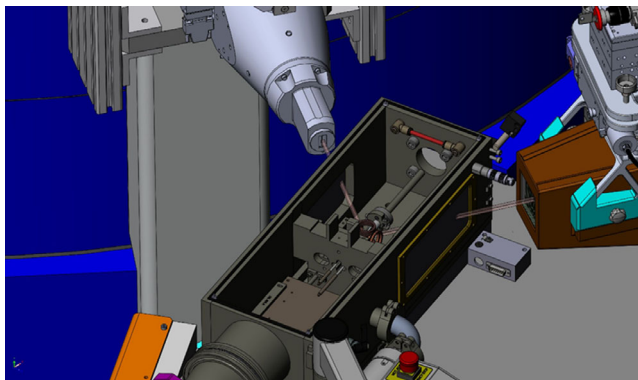


**Figure 3.** Schematic drawing showing the dilatometer and the beam defining optics at STRESS-SPEC. The slits in the incoming beam and the radial collimator in front of the detector define a measurement gauge volume of  $5 \times 5 \times 5 \text{ mm}^3$  located in the sample center.

coverage of  $15^\circ$  was used to record the diffraction patterns of the samples.<sup>[24]</sup> This 2D detector can be moved to cover a total  $2\theta$  angle ranging from  $40^\circ$  to  $100^\circ$ . Depending on the scattering properties of the specimen material, 10 to 30 s measuring time is needed for one diffractogram with one detector setting during an in situ measurement.

### 2.3. Operation and Data Acquisition

The temperature of the sample is programmed by the software Win-TA. Each activity such as heating and cooling is defined as a segment. The whole heat treatment process must be predefined in Win-TA. The parameters recorded during the experiment will be output to the instrumental server through a “start server” function, and are saved into a log file simultaneously with the measured STRESS-SPEC data. During the measurement, the temperature–time–length (TTL) curve can also be recorded synchronously with the in-house data acquisition system NICOS.<sup>[26]</sup> After the experiment is started, the only command that can be issued to the dilatometer through the NICOS system is the trigger signal “move to the next segment.” The purpose of this command is to synchronize the segments in the dilatometer experiment with the neutron diffraction images.

## 3. Examples of Application

The neutron dilatometer has been successfully commissioned at STRESS-SPEC in 2018, and it is now open for user service through the official MLZ proposal submission system. The following three examples will present recent measurements using

the dilatometer combined with in situ neutron diffraction of a cast iron alloy, an Mg–Al alloy, and a high entropy alloy (HEA), demonstrating the advantages of the synergy of both techniques.

### 3.1. Phase Transformation in Austempered Ductile Iron

Dilatometry has been used to study austenite to ferrite transformation kinetics in different kinds of ferrous alloys for many years.<sup>[1,27–29]</sup> A large number of essential information on the Fe–C phase diagram, such as the proeutectoid ferrite formation temperature  $A'_{f3}$ , the eutectoid start/finish transformation temperatures  $(A'_{f1})_s/(A'_{f1})_f$ , and phase transformation mode can be obtained directly through the TTL curve analysis.<sup>[1,27–29]</sup> However, additional diffraction data are in some cases essential to identify peculiarities in the phase transformation kinetics shown here, using as an example, the phase transformation and carbon diffusion process in Mo alloyed austempered ductile iron (ADI).

In ADI, the austenite to ferrite transformation is affected by carbon diffusion and takes place during the austempering process between 250 and 450 °C.<sup>[30,31]</sup> This kind of phase transformation is also defined as stage I reaction in ADI material. After a certain time and dependent on temperature, the carbon enriched retained austenite further decomposes into ferrite and cementite in the so-called stage II reaction. Between stages I and II, there is a processing window period, which lasts from 0 min to 3 h, depending on the austempering temperature and alloying elements content (i.e., Cu, Ni, and Mo).<sup>[32–35]</sup>

The change of the phase fractions of austenite and ferrite as well as the carbon redistribution, as encoded in the crystal lattice expansion of austenite, can be extracted from the diffraction profiles and length change curves (**Figure 4** and **5**).<sup>[20,21]</sup> At the beginning/end of stage I (**Figure 4a,c**), the reflections are symmetric and can be fitted using a single Gaussian peak shape function. In the middle part of stage I, the austenite Bragg reflections show an asymmetric shape caused by both, low carbon enriched and high carbon enriched austenite (**Figure 4b**).<sup>[30]</sup> The integrated peak intensities after fitting were used to quantify the phase fractions of austenite and ferrite.<sup>[30,31]</sup> The lattice constant of austenite calculated from the Bragg peak position of the (111) peak of austenite is shown together with the austenite phase fraction and the macroscopic length change recorded in the dilatometer in **Figure 5**.

During the first 3 h of austempering at 350 °C (**Figure 5a**), only the stage I reaction and beginning of the processing window in ADI materials can be characterized. The increase in sample length is related both to ferrite formation and carbon enrichment in retained austenite.<sup>[23]</sup> As shown by **Figure 5a**, the maximum of

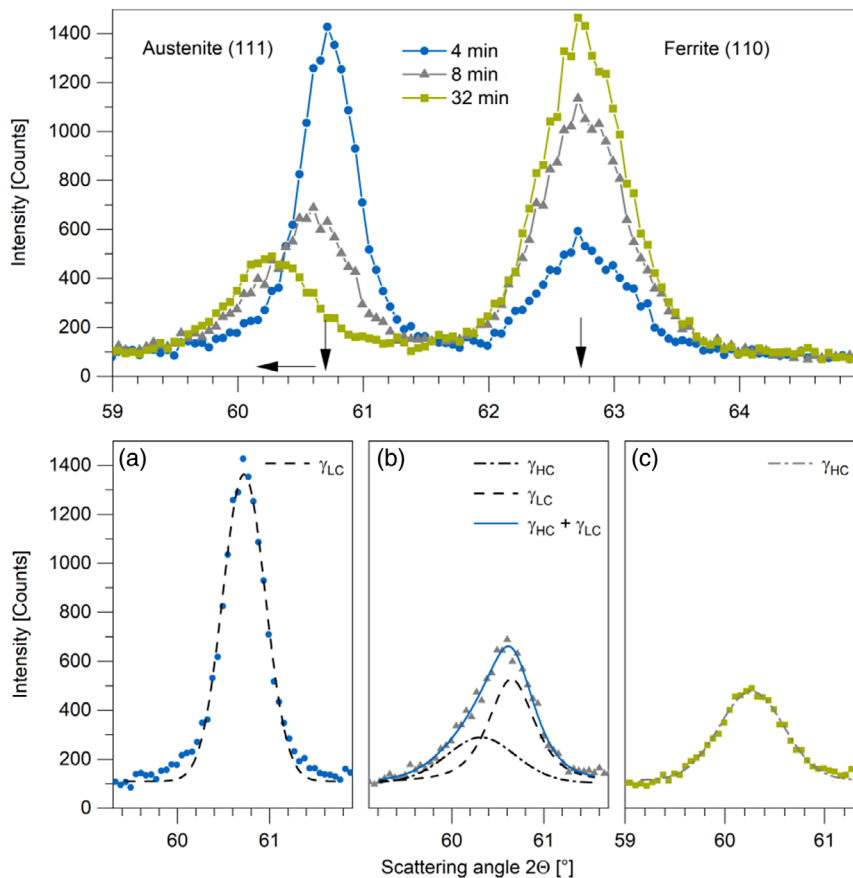


**Figure 4.** Austenite (111) and ferrite (110) Bragg reflections after austempering at 350 °C for 4, 8, and 32 min, respectively. a) Peak shape analysis of the austenite (111) Bragg reflection after 4 min of austempering, b) after 8 min, and c) after 32 min.  $\gamma_{LC}$ : low-carbon austenite,  $\gamma_{HC}$ : high-carbon austenite.

carbon enrichment in retained austenite is reached after the finish of austenite to ferrite transformation (stage I reaction). At the higher austempering temperature of 400 °C, the maximum of carbon enrichment is reached again after the end of stage I phase transformation, as shown in Figure 5b.<sup>[33]</sup> This shows that it is impossible to determine whether the phase transformation or carbon diffusion has been completed using dilatometry alone and additional informations from diffraction are essential. At the same time, the length change curve cannot be used directly for quantitative phase calculation, as it is additionally affected by carbon diffusion. In the sample austempered at 400 °C (Figure 5b), retained austenite decomposes into carbides and ferrite at increasing rate after the processing window. However, the expected positive length change resulting from austenite decomposition cannot be observed in the length change curve. This might be due to contraction effects of precipitating carbides or forming residual stresses, making it difficult to use the dilatometry results alone when studying phase transformations during which opposing effects occur.

### 3.2. Precipitation Kinetics in Mg–Al Binary Alloy

The Mg–Al–Zn (AZ) series of magnesium alloys based on the Mg–Al binary is one of the most popular magnesium alloys

for industrial applications due to its good castability. The maximum solubility of Al in Mg decreases with temperature from 12.7 wt% at 437 °C to 3 wt% at 200 °C.<sup>[36]</sup> To enhance the mechanical properties of Mg–Al alloy, a supersaturated Mg–Al alloy is usually subjected to a T6 isothermal aging heat treatment. In the selected aging temperature range from 150 to 250 °C, the  $\beta$ -phase ( $Mg_{17}Al_{12}$ ) has been found to be the only precipitate in Mg–Al alloys.<sup>[37]</sup> The precipitation process can be either continuous or discontinuous, depending on aging temperature and Al content.<sup>[36,38]</sup>

Since the density of  $\beta$ -phase precipitates is larger than that of pure Mg, it should be possible to observe a reduced length change in the TTL curve during the precipitation process.<sup>[38]</sup> At the same time, the occurrence of peaks from precipitates can also be observed in corresponding diffraction patterns. Due to the nanometer-sized  $\beta$ -phase precipitates and the phase detection limits (around 1 vol% of the phase) using in situ neutron diffraction technique, the information about the early stage of the precipitation process (nucleation) including the start point of precipitation at different aging temperatures might be lost in the continuously recorded neutron diffraction patterns.<sup>[39]</sup> Thus, the additional input from dilatometry makes up for this lack of experimental signal in the diffraction study of the early stage of precipitation.

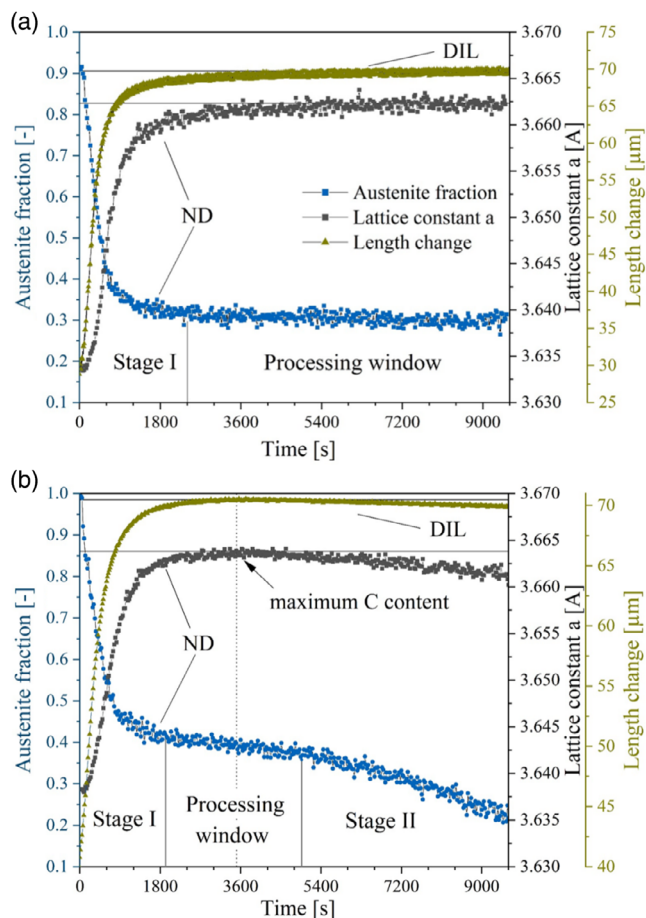


**Figure 5.** The phase fraction, lattice constant change of austenite, and TTL curves of ADI during austempering, a) at 350 °C for 3 h and b) at 400 °C for 3 h. ND: results from neutron diffraction. DIL: length change signal from dilatometer. Reproduced with permission of the CC-BY license.<sup>[33]</sup> Copyright 2020, The Authors, published by Licensee MDPI, Basel, Switzerland.

Another noted fact is that the homogeneous continuous precipitation will increase the lattice parameter of Mg overall in the matrix and discontinuous precipitation will cause a local increase of Mg lattice parameter near grain boundaries. This difference leads to a phenomenon that, on the one hand, the peak positions of Mg matrix will shift to smaller diffraction angles during continuous precipitation while the peak shape will become asymmetric during discontinuous precipitation, and on the other hand, an increased length change in the sample will be observed in the TTL curve during continuous precipitation. After theoretical quantitative calculation, it has been confirmed that the expansion caused by a lattice parameter change in the Mg matrix during continuous precipitation can completely compensate the contraction caused by precipitates, resulting in an overall macroscopic expansion of the sample.<sup>[38]</sup> Therefore, if the precipitation process is dominated by continuous precipitation, the length change signal will increase, and vice versa. Therefore, it is clear that to obtain detailed information on the precipitation process of Mg–Al alloy, a combination of dilatometer results with in situ neutron diffraction measurements is essential.

In Figure 6a,c,e, Bragg reflection intensity of the  $\beta$ -phase first appeared clearly in the neutron diffraction patterns after aging at 200 °C for 860 min, at 225 °C for 120 min, and at 250 °C for 50 min, respectively. However, at the beginning of aging, the decline in the corresponding TTL curves from the dilatometer (Figure 6b,d,f) indicates clearly that discontinuous precipitation occurred simultaneously in the aging process and dominated the precipitation in the early stage of isothermal aging. The peak shift of the Mg matrix to smaller  $2\theta$  values during aging (Figure 6a,c,e) shows that continuous precipitation also occurs at a certain time in the aging process. The possibility to exactly define the transition point of precipitation being dominantly discontinuous to continuous is an advantage when combining dilatometry with neutron diffraction.

In addition, taking Figure 6c as an example, although a diffraction signal of the precipitates can be found in the diffraction pattern after aging for 120 min, the Bragg intensity of the precipitates in the patterns is still too weak for quantitative phase analysis up to 300 min of aging. After combining the TTL curves from the whole aging process (10 h) and the phase fraction obtained from peak intensity analysis (after 300 min), the phase fraction of the precipitates in the early stage (<300 min) could be recalculated.<sup>[27–29]</sup>

### 3.3. Phase Transformation in HEAs

A difficulty in development of new HEAs results from the lack of specific information on the phases in the alloying system such as for instance their amount, exact chemical composition, or atomic site occupation numbers of each phase in the alloys.<sup>[40]</sup> This makes quantitative phase analysis using diffraction patterns and further in-depth study of phase transformations kinetics quite difficult. Therefore, research on HEAs focuses mainly on mechanical properties and microstructures.<sup>[41,42]</sup> In the absence of prior in-depth research results on the phase transformations kinetics of an alloying system, studying the relationship between its mechanical properties and microstructure and designing alloys with potential for industrial applications is time consuming and cost intensive. Therefore, a common method to obtain the phase composition of an alloying system is to apply thermodynamic analysis based on first principal calculations with dedicated software such as Thermo-Calc.<sup>[43]</sup> Unfortunately, previous studies have shown that results from Thermo-Calc calculations, such as, for example, phase compositions, phase transformation temperature, and chemical compositions of phases differ to some extent from experiment results.<sup>[44–46]</sup> However, combining dilatometry measurements with in situ neutron diffraction data, the phase transformation type and transformation temperature of HEAs can be determined conveniently from an analysis of the length change signal from dilatometry, and the integrated peak intensity and peak position change from in situ neutron diffraction measurements. Thus, an approach using thermodynamic calculations with combined neutron diffraction and dilatometry can substantially reduce the efforts in the development of new HEA systems.

Figure 7a shows the phase components predicted using Thermo-Calc, for an AlCrFeNiTi alloy produced through hot isostatic pressing (HIP), from 0 °C up to the melting point. Its result

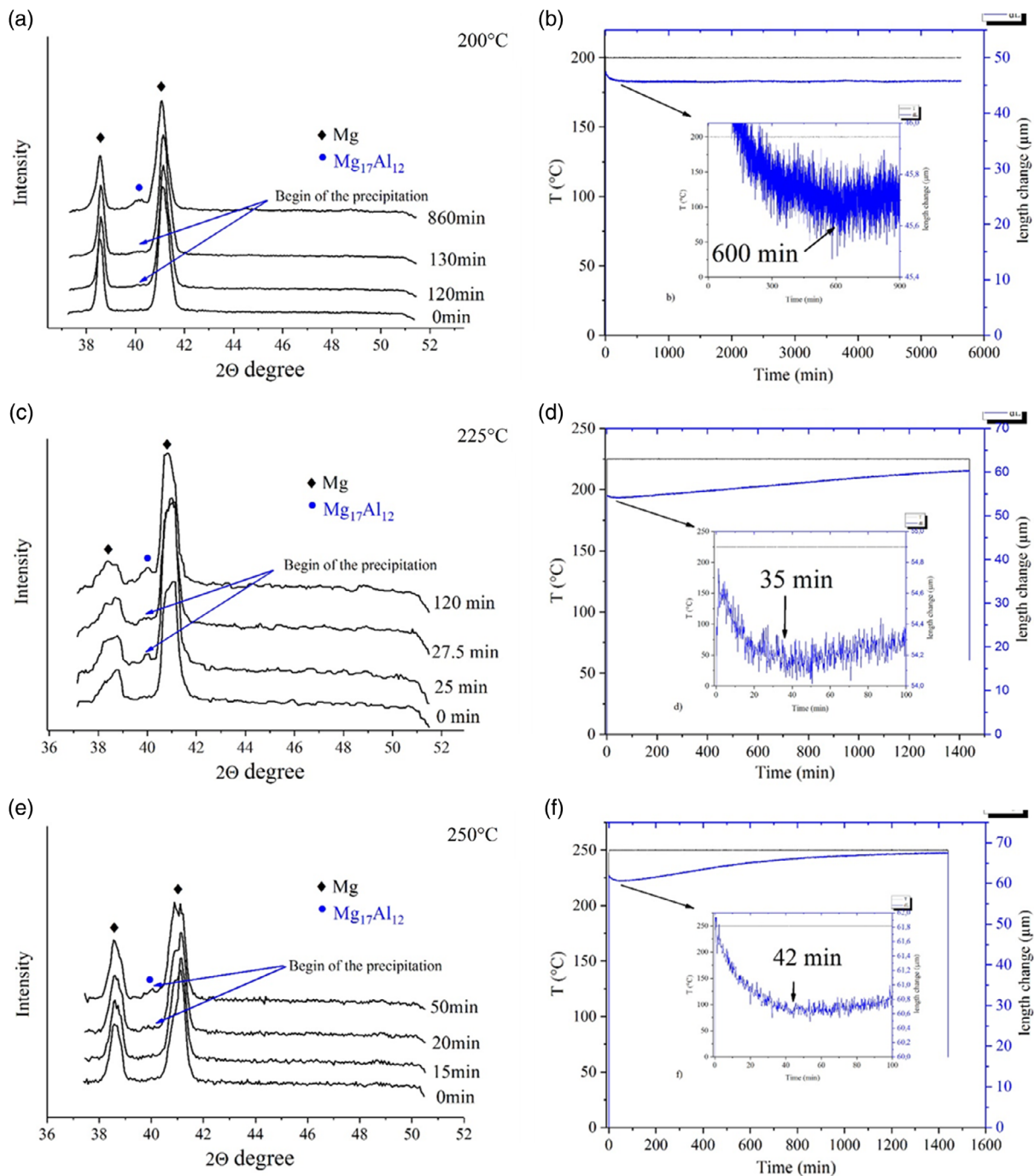


**Figure 6.** Neutron diffraction patterns and temperature–length change curves of Mg–8.9Al during aging a,b) at 200 °C, c,d) at 225 °C, and e,f) at 250 °C. Reproduced under terms of the CC-BY license.<sup>[38]</sup> Copyright 2019, The Authors, published by JOM.

depicts a complicated multiphase system consisting of more than ten different phases. The phase components obtained from electron backscatter diffraction (EBSD) and neutron diffraction measurements (**Figure 8**) in contrast differ significantly from the calculated phase diagram in **Figure 7a**. The experimental results indicate that the alloy AlCrFeNiTi consists mainly of three phases denoted as face-centered cubic (*fcc*)-L12, sigma, and body-centered cubic (*bcc*) from RT up to its melting point.<sup>[32]</sup> The

amount of these three phases is highlighted in the phase diagram in **Figure 7b** as phase fraction. The difference between the experiment and the calculated phase diagram has been further confirmed by other experimental results.<sup>[45]</sup>

In addition to predicting the possible phase compositions, Thermo-Calc also provides additional thermodynamic information on the AlCrFeNiTi alloying system as follows: 1) The amount of phase *fcc*-L12#2 starts to decrease gradually at 750 °C until it

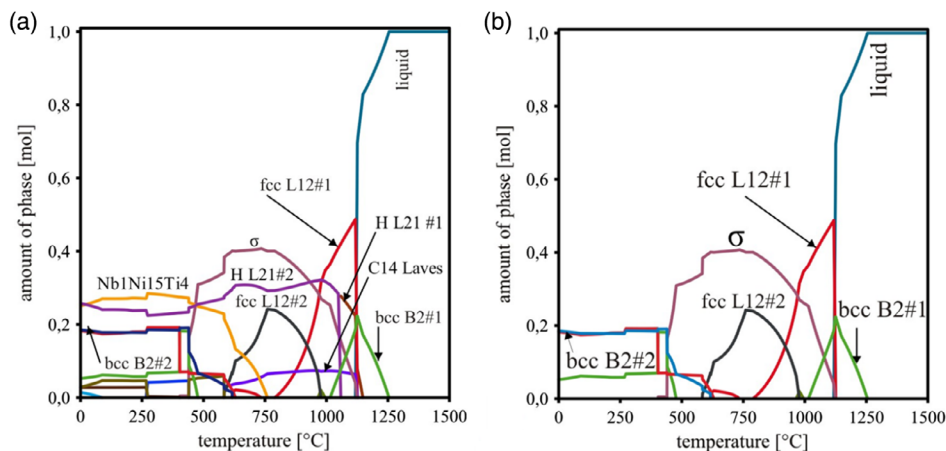


**Figure 7.** a) The phase diagram of AlCrFeNiTi alloy calculated by Thermo-Calc. b) The same phase diagram showing only the experimentally observed phases marked in color (i.e., *fcc*-L12, *sigma*, and *bcc* as discussed in the text).

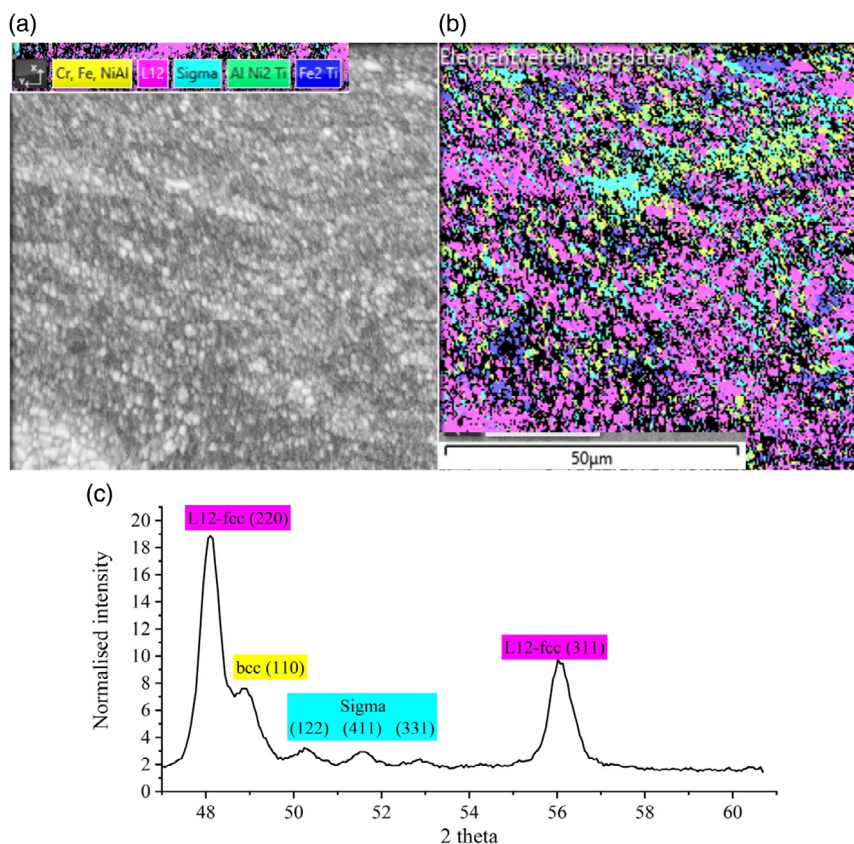


**Figure 8.** a) Scanning electron microscope micrograph of the AlCrFeNiTi alloy. b) The corresponding EBSD micrograph of the AlCrFeNiTi alloy. c) Neutron diffraction pattern of the AlCrFeNiTi alloy taken at 700 °C. In the in situ measurements, a wavelength 1.712 Å was selected with a Ge(311) monochromator and a gauge volume of  $5 \times 5 \times 5 \text{ mm}^3$  was set using a radial collimator setup. With this condition, the resolution in the diffraction profile is  $\Delta d/d = 0.005 - 0.007$ .

disappears completely at 1000 °C. The phase *fcc*-L12#1 forms at 800 °C and its amount increases up to the melting temperature of the alloy. 2) The amount of *sigma* phase starts to decrease at about 800 °C until it disappears completely at melting point. 3) *Bcc* B2#1 phase forms at about 1000 °C, its amount increases until the

melting point is reached, then it begins to melt until it disappears at 1250 °C. 4) No information about the type of phase transformation can be obtained by the Thermo-Calc simulations.

Therefore, to verify whether the information obtained from the calculated phase diagram in Figure 7b is consistent with



the actual experiment results and to identify the phase transformation type acting between these three phases, an in situ neutron diffraction experiment has been performed on an AlCrFeNiTi sample at STRESS-SPEC using the dilatometer to stepwise heat the sample and monitor the corresponding macroscopic length changes (Figure 9a).

The integrated peak intensity of each observed phase  $I_p$  was extracted after Gaussian peak fitting using the software STECA and was normalized according to Equation (1) for further comparison. The normalized peak intensity of the main phases is shown as a function of time in Figure 9b.

$$\text{Peak intensity change in [\%]} = 100\% \times \frac{I_p}{I_{p(0)}} \times k(T) \quad (1)$$

$I_p$ : Integrated peak intensity of one phase during the in situ measurement;  $I_{p(0)}$ : integrated peak intensity of one phase at the beginning of heat treatment; and  $k(T)$ : correction factor with consideration of the Debye–Waller factor.<sup>[47]</sup>

Although the Debye–Waller factors of the phases are unknown, one can use the summarized integrated intensity from the whole sample at different temperatures to calculate the  $k(T)$ .

In addition, the peak position obtained from the fitting was used to calculate the lattice parameter variations of each phase with the results shown in Figure 9c. According to the information obtained from peak intensity and lattice parameter evolution with temperature and time as shown in Figure 9b,c, the heat treatment temperature range can be divided into following three regions, yielding valuable insight into the phase transformation behavior:

In these temperature regions, the three phases *fcc*-L12, sigma, and *bcc* are always present and no other phases form. 1) First region (700 to 750 °C): *bcc* and *fcc*-L12 phases transform simultaneously into sigma phase, whereas the lattice parameters of both phases decrease slightly with holding time. This indicates that a diffusion controlled phase transformation or continuous precipitation should occur. The observations of peak location shift during in situ measurement at constant temperature are mainly caused by the diffusion in/out of matrix.<sup>[48,49]</sup> When this process is also time dependent, the occurrence of diffusion controlled transformation should be considered to take place. 2) Second region (750 to 850 °C): *fcc*-L12 phase starts to further transform into two phases, *bcc* and sigma. This transformation process is dependent on time and temperature, indicating that a typical diffusion controlled transformation is taking place in this temperature region. The thermal lattice expansion caused by rapid heating can only be observed in the *fcc* and *bcc* phases, but not in sigma phase Figure 9a,c. At 750 °C, the lattice parameters *a* and *c* of sigma phase show an opposite change, and remain almost constant up to 900 °C. A possible explanation for this observation may be the following: the new *bcc* phase that evolves from the *fcc* phase has the same chemical composition as the parent *bcc* phase, and surplus atoms from *fcc* phase will diffuse into the sigma phase thereby changing its chemical composition, resulting in the observed change of lattice parameters of this phase. 3) Third region (900C to 1050 °C): Above 900 °C, an increased length change and an oscillating trend for *bcc* and sigma phases can be observed in Figure 9a,b, respectively. This seems to reveal that a massive phase transformation takes

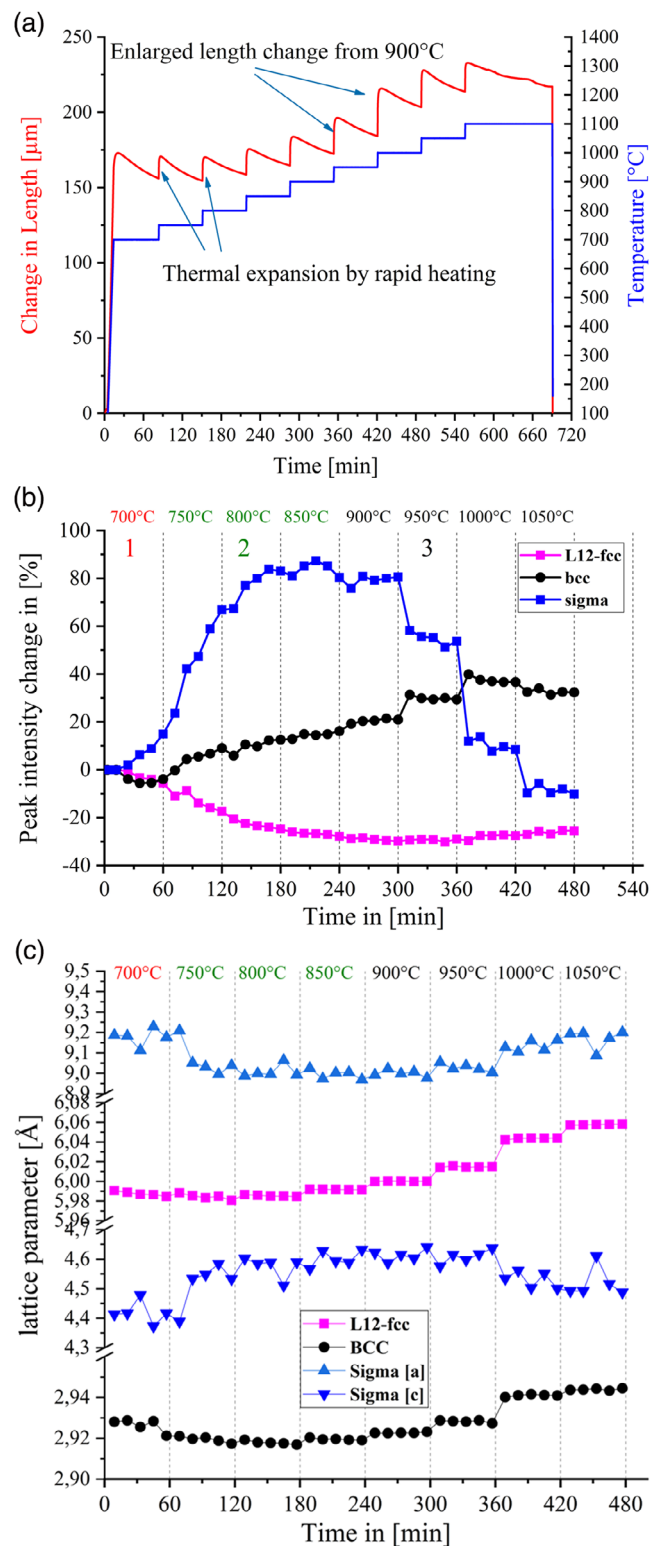


**Figure 9.** a) The TTT curve of the heat treatment process during the in situ neutron diffraction experiment. b) Evolution of peak intensity of *fcc*-L12, sigma, and *bcc* phases in AlCrFeNiTi during the heat treatment. c) Lattice parameter change of *fcc*-L12, sigma, and *bcc* phases in AlCrFeNiTi during the heat treatment.

place in this temperature range where sigma phase transforms back into *bcc* phase whereas the *fcc* phase remains unchanged.

The phase transformation principle seen in this alloy indicates that when two phases undergo a transformation in a certain temperature range, the type of phase transformation will not change. The type of phase transformation between *fcc*-L12, sigma, and *bcc* phases in the AlCrFeNiTi alloying system is confirmed to be dependent on temperature, in this case at about 900 °C, which is a new discovery made in this alloying system.

## 4. Conclusion

From the three examples shown earlier, the advantages of combining dilatometry with in situ neutron diffraction can be summarized as follows: 1) The addition of the dilatometer compensates to a certain extent for the low time resolution of the in situ neutron diffraction measurement in the study of phase transformations. Some rapid phase transformation phenomena such as massive transformation in HEAs and the related phase transformation temperature can be directly observed in the TTL curves provided by the dilatometer. 2) The high-resolution length change signal of the dilatometer exhibits a resolution much higher than that of neutron diffraction in quantitative phase analysis, which provides additional accurate data for studying nucleation processes and slow precipitation. 3) The combination of dilatometry and neutron diffraction bundles various advantages in one in situ measurement such as high time resolution, high length change accuracy, precise temperature control, large gauge volume, microstructural analysis, and crystallographic insight. Several important parameters in phase transformation studies such as start/end point of transformation, transformation temperature, transformation type, and transformation rate can thus be obtained within a single measurement setup.

## Acknowledgements

Open access funding enabled and organized by Projekt DEAL.

## Conflict of Interest

The authors declare no conflict of interest.

## Data Availability Statement

The data that support the findings of this study are openly available at <https://doi.org/10.1007/s11837-019-03516-6> and [doi:10.3390/ma13225266](https://doi.org/10.3390/ma13225266), reference number [23, 28].

## Keywords

dilatometer, engineering materials, neutron diffraction, phase transition

Received: February 6, 2021

Revised: March 25, 2021

Published online:

- [1] Y. Z. Zhan, Y. Du, Y. H. Zhuang, in *Methods for Phase Diagram Determination* (Ed.: J.-C. Zhao), 1st ed., Elsevier Science Ltd, Amsterdam **2007**, pp. 108–150.
- [2] TA Instruments, DIL 831 specifications, <https://www.tainstruments.com/dil-831/> (accessed: February 2021).
- [3] A. Grajcar, *J. Therm. Anal. Calorim.* **2014**, *118*, 739.
- [4] E. Pereloma, D. V. Edmonds, *Phase Transformations in Steels, Volume 1 Fundamentals and Diffusion-Controlled Transformations*, Woodhead Publishing Ltd, Philadelphia, USA **2012**, p.143.
- [5] C. García de Andrés, F. G. Caballero, C. Capdevila, L. F. Álvarez, *Mater. Charact.* **2002**, *48*, 101.
- [6] V. Voort, F. George, *Atlas of Time-Temperature Diagrams for Irons and Steels*, ASM International, Metals Park, OH **1991**.
- [7] R. Enzinger, E. Hengge, W. Sprengel, R. Würschum, *J. Mater. Sci.* **2019**, *54*, 5083.
- [8] V. Recarte, R. B. Pérez-Sáez, M. L. No, J. San Juan, *J. Phys. IV France* **1997**, *7*, 329.
- [9] C. Garcia-Mateo, F. G. Caballero, C. Capdevila, C. Garcia de Andres, *Scr. Mater.* **2009**, *61*, 855.
- [10] A. Stark, M. Rackel, T. A. Tchouaha, M. Oehring, N. Schell, L. Lottermoser, A. Schreyer, F. Pyczak, *Metals* **2015**, *5*, 2252.
- [11] E. J. Pickering, J. Collins, A. Stark, L. D. Connor, A. A. Kiely, H. J. Stone, *Mater. Charact.* **2020**, *165*, 110355.
- [12] D. Tolnai, C. L. Mendis, A. Stark, G. Szakács, B. Wiese, K. U. Kainer, N. Hort, *Mater. Lett.* **2013**, *102–103*, 62.
- [13] P. Erdely, T. Schmoelzer, E. Schwaighofer, H. Clemens, P. Staron, A. Stark, K.-D. Liss, S. Mayer, *Metals* **2016**, *6*, 10.
- [14] P. Staron, T. Fisher, T. Lippmann, A. Stark, S. Daneshpour, D. Schnubel, E. Uhlmann, R. Gerstenberger, B. Camin, W. Reimers, E. Eidenberger, H. Clemens, N. Huber, A. Schreyer, *Adv. Eng. Mater.* **2011**, *13*, 658.
- [15] Y. Q. Wang, S. Kabra, S. Y. Zhang, C. E. Truman, D. J. Smith, *Rev. Sci. Instrum.* **2018**, *89*, 055110.
- [16] K. An, H. D. Skorpenske, A. D. Stoica, D. Ma, X. L. Wang, E. Cakmak, *Metall. Mater. Trans.* **2011**, *A42*, 1, 95.
- [17] A. Shibata, Y. Takeda, N. Park, L. J. Zhao, S. Harjo, T. Kawasaki, W. Gong, N. Tsuji, *Scr. Mater.* **2019**, *165*, 44.
- [18] D. D. Ma, P. Yang, X. F. Gu, Y. Onuki, S. Sato, *Mater. Charact.* **2020**, *163*, 110244.
- [19] D. E. Nicholson, S. A. Padula, O. Benafan, J. R. Bunn, E. A. Payzant, K. An, D. Penumadu, R. Vaidyanathan, *Adv. Mater.* **2021**, *33*, 2005092.
- [20] Y. X. Wang, Y. Tomota, T. Ohmura, S. Morooka, W. Gong, S. Harjo, *Acta Mater.* **2020**, *184*, 30.
- [21] O. Yusuke, H. Takashi, H. Akinori, S. Shigeo, T. Toshiro, *Metall. Mater. Trans.* **2019**, *A50*, 4977.
- [22] [https://mlz-garching.de/media/dilatometer-sans-1\\_en.pdf](https://mlz-garching.de/media/dilatometer-sans-1_en.pdf).
- [23] <https://www.tainstruments.com/dil-805adt-queenching-dilatometers/>.
- [24] M. Hofmann, G. A. Seidl, J. R. Kornmeier, U. Garbe, R. Schneider, R. C. Wimpory, U. Wasmuth, U. Noster, *Mater. Sci. Forum* **2006**, *524–525*, 211.
- [25] M. Hoelzel, W. M. Gan, M. Hofmann, C. Randau, G. Seidl, Ph. Jüttner, W. W. Schmahl, *Nucl. Instrum. Meth. Phys. Res.* **2013**, *A711*, 101.
- [26] T. Unruh, in *Proc. of the NOBUGS 2002 Conf.*, **2002**, arXiv: cond-mat/021043.
- [27] M. Gómez, S. F. Medina, G. Caruana, *ISIJ Inter.* **2003**, *43*, 1228.
- [28] T. A. Kop, J. Sietsma, S. V. D. Zwaag, *J. Mater. Sci.* **2001**, *36*, 519.
- [29] Y. C. Liu, D. J. Wang, F. Sommer, E. J. Mittemeijer, *Acta Mater.* **2008**, *56*, 3833.
- [30] L. Meier, M. Hofmann, P. Saal, W. Volk, H. Hofmann, *Mater. Charact.* **2013**, *85*, 124.
- [31] X. H. Li, J. N. Wagner, A. Stark, R. Koos, M. Landesberger, M. Hofmann, G. H. Fan, W. M. Gan, W. Petry, *Metals* **2019**, *9*, 789.

- [32] P. Saal, L. Meier, X. H. Li, M. Hofmann, M. Hoedel, J. N. Wagner, W. Volk, *Metall. Mater. Trans. A* **2016**, *47*, 661.
- [33] M. Landesberger, R. Koos, M. Hofmann, X. H. Li, T. Boll, W. Petry, W. Volk, *Materials* **2020**, *13*, 52.
- [34] Z. Ławrynowicz, *Adv. Mater. Sci.* **2016**, *16*, 47.
- [35] O. E. Cekic, L. Sidjanin, D. Rajnovic, S. Balos, *Met. Mater. Int.* **2014**, *20*, 1131.
- [36] K. N. Braszczyńska-Malik, *J. Alloy. Compd.* **2009**, *477*, 870.
- [37] J. F. Nie, *Metall. Mater. Trans.* **2012**, *A43*, 3891.
- [38] X. Zhang, Y. D. Huang, X. H. Li, W. M. Gan, K. U. Kainer, N. Hort, *JOM* **2019**, *71*, 2906.
- [39] A. G. de la Torre, A. Cabeza, A. Calvente, S. Bruque, M. A. G. Aranda, *Anal. Chem.* **2001**, *73*, 151.
- [40] Y. F. Ye, Q. Wang, J. Lu, C. T. Liu, Y. Yang, *Mater. Today* **2016**, *19*, 349.
- [41] B. S. Murty, J. W. Yeh, S. Ranganathan, P. P. Bhattacharjee, *High-Entropy Alloys*, 2nd ed., Elsevier, Amsterdam **2019**.
- [42] M. Reiberg, J. von Kobylinski, E. Werner, *Continuum Mech. Thermodyn.* **2020**, *32*, 1147.
- [43] Thermo-Calc Software AB, "Thermo-Calc Version 2020a (Thermo-Calc Documentation Set)", <https://www.thermocalc.com/support/documentation/> (accessed: May 2020).
- [44] A. Takeuchi, *Mater. Trans.* **2020**, *61*, 1717.
- [45] L. Liu, R. Paudel, Y. Liu, X. L. Zhao, J. C. Zhu, *Materials* **2020**, *13*, 4353.
- [46] A. Munitz, S. Salhov, G. Guttman, N. Derimow, M. Nahmany, *Mater. Sci. Eng.* **2019**, *A742*, 1.
- [47] D. B. Sirdeshmukh, L. Sirdeshmukh, K. G. Subhadra, in *Micro- and Macro-Properties of Solids*, Materials Science, Vol. 80, Springer, Berlin, Heidelberg, **2006**, pp. 77–133.
- [48] S. S. Babu, E. D. Specht, S. A. David, E. Karapetrova, P. Zschack, M. Peet, H. K. D. H. Bhadeshia, in *Proc. of the 1st Int. Symp. on Steel Science (IS3-2007)*, **2007**, pp. 93–99.
- [49] Z. Tournoud, F. De Geuser, G. Renou, D. Huin, P. Donnadieu, A. Deschamps, *Quantum Beam Sci.* **2019**, *3*, 25.